

A model for the fragmentation kinetics of crumpled thin sheets

Jovana Andrejevic,¹ Lisa M. Lee,¹ Shmuel M. Rubinstein,¹ and Chris H. Rycroft^{1,2}

¹*John A. Paulson School of Engineering and Applied Sciences,
Harvard University, Cambridge, MA 02138, USA*

²*Computational Research Division, Lawrence Berkeley Laboratory, Berkeley, CA 94720, USA*
(Dated: November 10, 2021)

As a confined thin sheet crumples, it spontaneously segments into flat facets delimited by a network of ridges. Despite the apparent disorder of this process, statistical properties of crumpled sheets exhibit striking reproducibility. Experiments have shown that the total crease length accrues logarithmically when repeatedly compacting and unfolding a sheet of paper. Here, we offer insight to this unexpected result by exploring the correspondence between crumpling and fragmentation processes. We identify a physical model for the evolution of facet area and ridge length distributions of crumpled sheets, and propose a mechanism for re-fragmentation driven by geometric frustration. This mechanism establishes a feedback loop in which the facet size distribution informs the subsequent rate of fragmentation under repeated confinement, thereby producing a new size distribution. We then demonstrate the capacity of this model to reproduce the characteristic logarithmic scaling of total crease length, thereby supplying a missing physical basis for the observed phenomenon.

I. INTRODUCTION

Crumpling is a complex, non-equilibrium process arising in diverse systems across a wide range of length scales, from the microscopic crumpling of graphene membranes [1], to the macroscopic folding of Earth's viscoelastic crust [2]. Crumpled structures are highly porous, providing function for applications such as high-performance batteries and supercapacitors by increasing the electrochemical surface area [3, 4]. Controlled crumpling has also been used to tune electronic, optical, and surface properties in graphene films [1]. Further, understanding the mechanics of crumpling is essential as flexibility and shape conformation become integral considerations in the design of thin, wearable devices [5, 6]. Despite its ubiquity, a complete understanding of crumpling dynamics remains elusive due to the complexity of the disordered process. Nevertheless, statistical properties of crumpled geometries are highly reproducible in experiment [7–13] and confirmed via simulation [14, 15], which suggests that this complex process is strongly dictated by universal aspects of thin sheets such as topology and self-avoidance [13].

Similarly adopting a coarse-grained perspective, Gottesman *et al.* [16] revealed an unexpected order to ridge network evolution in crumpled sheets. By performing a protocol of repeated compaction and unfolding, as in the schematic of Fig. 1(a), they demonstrated that the intricate details of ridge networks in crumpled sheets could be reduced to a single collective quantity, the total crease length, which evolves robustly as a logarithm in the number of crumpling repetitions across varying degrees of compaction. Notably, the incremental damage added was found to be independent of the sheets' crumpling history, determined only by the current total crease length and the new compaction depth. While processes that evolve logarithmically in time are readily observed in a variety of disordered physical systems, including stress or strain relaxation of a compacted sheet [17–19], conductance relaxation of disordered electronic systems [20], and creep

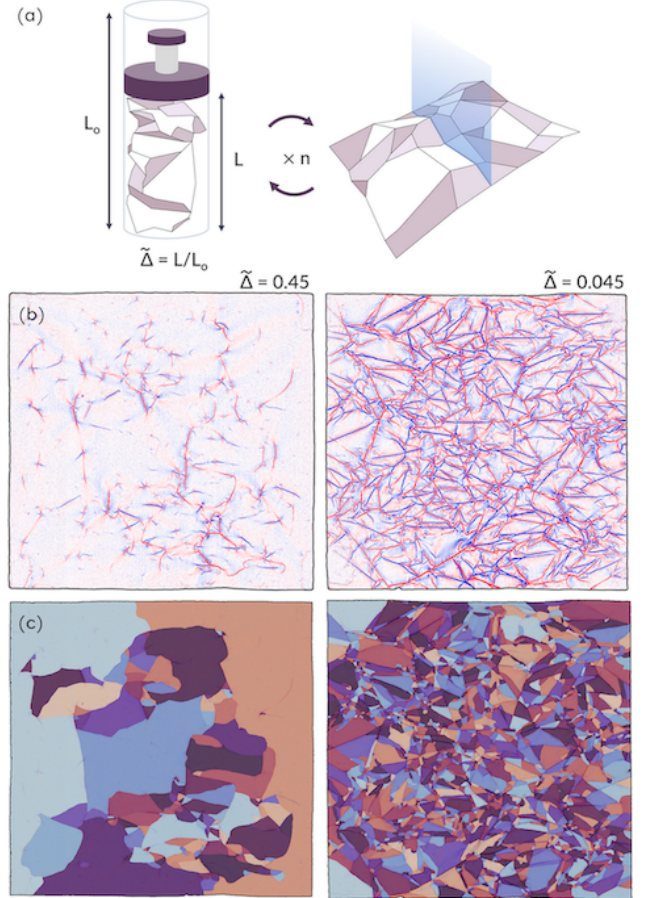


FIG. 1. (a) An $L_0 \times L_0$ Mylar sheet is compressed uniaxially to a compaction ratio $\tilde{\Delta} = L/L_0$, unfolded, and its height profile scanned using a laser profilometer, for n iterations. (b) The mean curvature obtained from the topographic information of two experimental examples. Red and blue colors denote folds in opposing directions. (c) The facet segmentation of (b), using random coloring for visual distinction between facets.

dynamics of granular suspensions [21], the emergence of a logarithmic model in the specific context of damage evolution in crumpled sheets is clearly distinct, and has had limited physical justification thus far.

In this work, we take a novel approach to characterize crumpling and offer explanation for the logarithmic model by drawing a correspondence between crumpling and fragmentation processes. Fragmentation models have a rich history of theoretical development [22–24] as well as industrial applications [22, 25] and use in modelling collision and fracture phenomena [26]. Here we concentrate on a theoretical, physically-based rate equation for modeling time-dependent fragmentation detailed by Cheng and Redner [27], which provides a general framework for processes that may be treated as successive, homogeneous breakups instigated by non-local stresses. The model has been flexibly applied to describe polymer degradation [28] and volcanic fragments expelled in an eruption [29], for example, though to the best of our knowledge this is the first application of such concepts to describe crumpling.

Our work is organized as follows: We derive a scaling solution to the rate equation presented in Ref. [27] which decomposes into a time-invariant distribution of scaled facet area and a time-dependent evolution of mean facet size. We demonstrate that the derived area distribution effectively reproduces key statistical features of experimental crumpled patterns. Fragment distributions are a natural point of comparison between theory and experiment; however, in this work we go a step further to draw additional correspondence in the temporal evolution of the patterns. The temporal parameter that chronicles the evolution of mean facet size serves as an intrinsic clock measuring the maturity of the fragmentation process. We connect this to experimental parameters driving fragmentation forward, namely the number of crumpling iterations and compaction strength which characterize the experiments of Ref. [16]. To do so, we construct a simple geometric model that likens crumpling to a random walk and is informed by the statistical properties of the derived area distribution. We derive an analytical relation for how geometric frustration occurring in a confined random walk instigates new damage and advances the temporal measure of fragmentation maturity. We demonstrate how this approach allows one to recover the logarithmic evolution of damage in ridge networks observed in Ref. [16] and explain the history independence of damage formation, thereby furnishing a missing physical basis for this unexpected result.

The key idea behind our model is the extension of fragmentation theory to incorporate a feedback loop: As facets become smaller, they make the sheet more compliant and therefore lower the rate of subsequent fragmentation. This idea may extend to many physical systems where the accumulation of damage inhibits further damage from occurring. Our work therefore shows how fragmentation theory could be applied more generally, and suggests that the universal damage evolution seen in crumpling may have analogs in other physical systems.

II. BACKGROUND

Throughout this work, we will refer to fragmentation in the context of crumpling as the successive partitioning of a thin sheet into smaller, flat facets separated by ridges or creases. To facilitate the construction of a model for this process, we begin with the general theory of fragmentation kinetics outlined in Ref. [27]. Let x represent facet area and $c(x, t)$ the concentration of facets of area x at time t ; then the linear integro-differential equation describing the evolution of $c(x, t)$ is given by

$$\frac{\partial c(x, t)}{\partial t} = -r(x)c(x, t) + \int_x^\infty c(y, t)r(y)f(x|y)dy, \quad (1)$$

where the effective time t measures the progress or maturity of the fragmentation process, $r(x)$ is the overall rate at which a facet of area x fragments, and $f(x|y)$ is the conditional probability that x is produced from the breakup of y , with $y \geq x$. Inferred from this formulation are the assumptions that fragmentation occurs via a homogeneously applied external force, and independently of a facet's shape.

III. EXPERIMENTAL DATA

The data analyzed in this work was collected for the study of Ref. [16]; here, we briefly summarize the experimental protocol for reference. 10 cm \times 10 cm Mylar sheets are rolled into a 3 cm diameter cylindrical container and compressed uniaxially to a specified compaction ratio $\hat{\Delta} = L/L_0$, the ratio of final to initial height, with $L_0 = 10$ cm (Fig. 1(a)). The resulting ridge network inscribed on each sheet is extracted by carefully unfolding and scanning the sheet using a custom laser profilometer, which produces a height map of the sheet. A two-dimensional map of mean curvature is determined from the spatial gradients of the height profile; sharp peaks in curvature mark the signature of a ridge (Fig. 1(b)). Successive re-crumpling and scanning of a single sheet is performed n times up to $n = 24$. Individual facets, characterized as contiguous regions of near-zero curvature, are delineated as shown in Fig. 1(c). Due to noise and artifacts in data collection, not all facets are completely enclosed by a contour of ridges; breaks along a ridge, or smoothing out and softening of ridges, occur inevitably during re-crumpling and unfolding. Automated methods of crease detection and facet labeling were initially tested to perform the segmentation; however, these methods proved sensitive to noise and thus were prone to over-fragmenting the sheets. Each sample presented and analyzed in this work was digitally labeled by hand. A comparison to automated segmentation is provided in Section II of the Supplemental Material [30]. Care was taken to identify not only the dominant lines of each pattern as seen in the examples, but also the less pronounced softer scarring. The segmentation was performed

for sheets after iterations $n = 1, 2$ and 3 at seven different compaction ratios: $\tilde{\Delta} = 0.63, 0.45, 0.36, 0.27, 0.18, 0.09$ and 0.045 . Each series of successive crumples was compared across all iterations n for consistency, to ensure that labeled facets from earlier iterations persist in later ones. Samples with $\tilde{\Delta} = 0.63, 0.45$, and 0.27 were also labeled after $n = 24$ crumples, for a total of 24 samples overall. We acknowledge that samples at $n = 24$ are more prone to missing detail as older scarring is obscured by newer ridges, but are nonetheless valuable to the study.

IV. ANALYTICAL SOLUTION

A. Breakup rates

In order to assess the correspondence between crumpling and a fragmentation process as described by Eq. (1), two relationships must be specified: the overall breakup rate $r(x)$, and conditional breakup probability $f(x|y)$, which characterize fragmentation at the scale of an individual facet. Two principles help shape our formulations of the two: Firstly, a common choice of $r(x)$ consistent with physical breakup processes is the homogeneous kernel $r(x) = x^\lambda$ [27]. Furthermore, the conditional probability $f(x|y)$ must satisfy area conservation:

$$\int_0^y x f(x|y) dx = y. \quad (2)$$

We use the collection of facets within each sheet as representative samples from which breakup rates may be determined. Fig. 2(a-c) shows a typical example over three crumpling repetitions and traces the progressive fragmentation of selected facets. From such sequences, we estimate $r(x)$ by determining the fraction of facets which fragment between two successive crumples as a function of their area x . The rates are computed separately for each sheet to ensure the same change in t elapses for all facets considered at a time. Without loss of generality, the values of x in all results are scaled so that $10 \text{ cm} \times 10 \text{ cm}$ corresponds to unit area. A breakup rate of the form $r(x) = x^\lambda$ appears consistent with experimental breakup data, as shown in Fig. 2(d).

To deduce $f(x|y)$ it is helpful to first examine the distribution $\rho(x/y)$ of the area fraction x/y that a *child* facet occupies relative to its *parent*. That is, if x is the area of a facet at crumpling iteration n , and y the area of its enclosing facet at iteration $n - 1$, then $\rho(x/y)d(x/y)$ is the probability that a facet breaks to produce a fragment that is between x/y and $x/y + d(x/y)$ of its initial area, for a small differential element $d(x/y)$. To account for minor misalignment between successive scans, a child facet is identified if at least half of its area lies within the contour of the candidate parent facet. The area fractions display a power law distribution, as shown in Fig. 2(e), and suggest

a fit to a probability density function of the form

$$\rho\left(\frac{x}{y}\right) = (\beta + 1)\left(\frac{x}{y}\right)^\beta, \quad (3)$$

supported on $x/y \in [0, 1]$. This formulation introduces the assumption that fragmentation is a scale invariant process; while this is consistent with the present data, we note that a physical lower limit on facet area exists, and would expect deviation from scale invariant behavior as facet areas become comparable to the sheet thickness. Further, we keep in mind two difficulties with our analysis: Weakly crumpled sheets may have too few facets for a robust sample size from which to build our distribution; in the opposing extreme, facets in strongly crumpled samples may undergo a succession of multiple fragmentation events in a single crumpling iteration, and thus may not resolve the behavior of a single facet. Despite these challenges, we observe clear indication of the described trends within our data, as shown in Fig. 2(e). Extended results are provided in Section II C and Figs. S5 and S6 of the Supplemental Material [30]. Taking $f(x|y)$ proportional to $\rho(x/y)$ and obtaining the appropriate normalization which satisfies Eq. (2), we arrive at our final forms for the breakup rates:

$$r(x) = x^\lambda, \quad (4a)$$

$$f(x|y) = \frac{1}{y} \left(\frac{\beta + 2}{\beta + 1} \right) \rho\left(\frac{x}{y}\right) = \frac{1}{y} (\beta + 2) \left(\frac{x}{y}\right)^\beta. \quad (4b)$$

It will prove useful to express the free parameter β as

$$\beta = \frac{a}{2} - 1. \quad (5)$$

With this definition, we demonstrate in Section V that the new free parameter a is closely related to the shape parameter for the distribution of crease length.

B. Scaling solution

With $r(x)$ and $f(x|y)$ specified, we pursue an analytical solution to the fragmentation rate equation (Eq. (1)). Specifically, we seek a scaling solution independent of initial conditions, a property that allows us to solve analytically and proves compatible with the chosen form of homogeneous breakup kernels [27]. We thereby test a scaling ansatz $c(x, t) = \phi(\xi)/s(t)^2$ as proposed in Ref. [27], where $\xi = x/s(t)$, and the mean area, $s(t)$, carries all explicit dependence on t . The scaling function $\phi(\xi)$ satisfies $\int_0^\infty \phi(\xi) d\xi = 1$ and $\int_0^\infty \xi \phi(\xi) d\xi = 1$ such that $\int_0^\infty c(x, t) dx = 1/s(t)$ gives the average number of fragments, and $\int_0^\infty xc(x, t) dx = 1$ is the total area, conserved by construction. We note that $\phi(\xi)$ is a valid probability density function and represents the distribution of the scaled facet area ξ . The rate equation may be solved following the procedure in Ref. [27] as detailed in Section I of the Supplemental Material [30]; by this approach we

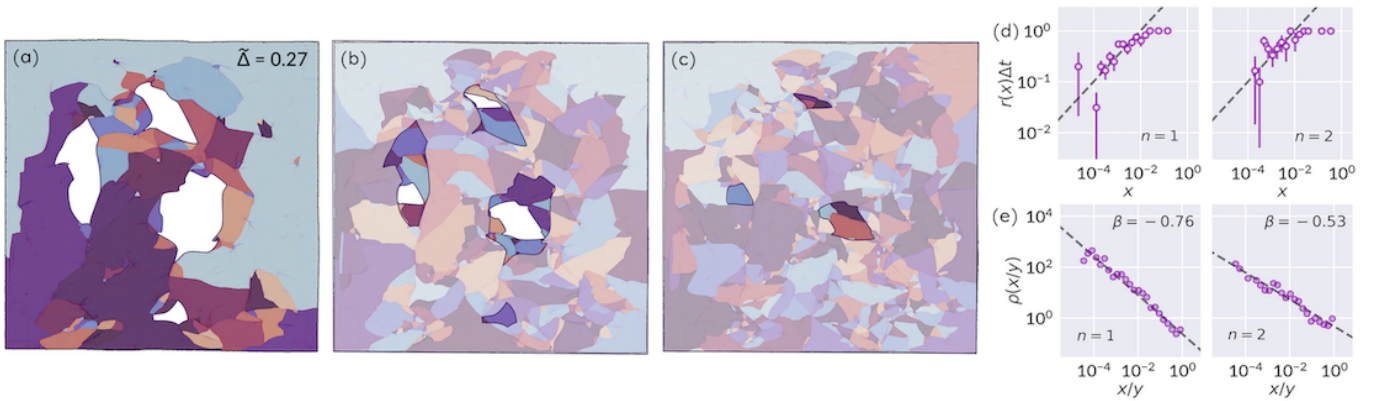


FIG. 2. (a) Segmentation of a sample sheet crumpled once at compaction $\bar{\Delta} = 0.27$, with four selected facets outlined in white. Shown in (b) are the new facets that subdivide those regions after crumpling a second time ($n = 2$). In (c), the subdivision of the facets highlighted in (b) is shown after $n = 3$. (d) For $n = 1$ (left), the proportion of facets $r(x)\Delta t$ present in (a) as a function of their area x , which have fragmented into at least two distinct facets in (b) over the elapsed Δt between $n = 1$ and $n = 2$. For $n = 2$ (right), the fraction of facets from (b) which have fragmented in (c). The dashed line corresponds to \sqrt{x} . (e) The probability density function $\rho(x/y)$ of facet areas x normalized by their parent facet's area y from the previous crumpling iteration. The $n = 1$ (left) panel is the distribution of area fractions for facets in (b) relative to their parent facets in (a), and $n = 2$ the corresponding distribution for facets in (c) relative to (b). The dashed line corresponds to a fit of Eq. (3) with the fitted exponent β given.

arrive at a solution $c(x, t) = \phi(\xi)/s(t)^2$, valid at large t , with

$$\phi(\xi) = \frac{\lambda}{\Gamma\left(\frac{\alpha}{2\lambda}\right)} G(a, \lambda) (G(a, \lambda)\xi)^{\frac{\alpha}{2}-1} e^{-(G(a, \lambda)\xi)^\lambda}, \quad (6a)$$

$$s(t) = G(a, \lambda)t^{-1/\lambda}, \quad (6b)$$

where $G(a, \lambda) = \Gamma\left(\frac{a+2}{2\lambda}\right)/\Gamma\left(\frac{a}{2\lambda}\right)$. A breakup rate parameter $\lambda = 1/2$ appears consistent across a wide range of our data, as shown in Fig. 2(d); thus we introduce a simplification to our model by fixing this value to obtain the final forms

$$\phi(\xi) = \frac{a(a+1)}{2\Gamma(a)} (a(a+1)\xi)^{\frac{a}{2}-1} e^{-\sqrt{a(a+1)\xi}}, \quad (7a)$$

$$s(t) = \frac{a(a+1)}{t^2}. \quad (7b)$$

V. DATA ANALYSIS

To facilitate comparison with $\phi(\xi)$ in Eq. (7a), the area of individual facets is scaled by the mean area for that sheet and plotted as a histogram using logarithmically spaced bins. Fig. 3 shows the distributions of experimental data and the corresponding best fit to Eq. (7a) using maximum likelihood estimation, with a as the fitting parameter. The complete set of distributions and fits to Eq. (7a) for all data samples are provided in Fig. S2 of the Supplemental Material [30].

A. Ridge length statistics

The close correspondence between Eq. (7a) and experimental data supports the hypothesis that successive partitioning of the sheet's surface into facets during crumpling evolves according to the fragmentation process described by Eq. (1). We can study the further implications of this statistical description on attributes such as the distribution of crease length, which has been explored in previous studies [7–10, 14, 15, 31]. Let X be the random variable representing the area of a single facet. Following from Eq. (7a), X is distributed as

$$f_X(x) = \frac{1}{2\theta^2\Gamma(a)} \left(\frac{x}{\theta^2}\right)^{\frac{a}{2}-1} e^{-\sqrt{x}/\theta}, \quad (8)$$

with $\theta = \sqrt{s/a(a+1)} = 1/t$ by consequence of Eq. (7b), and mean area s . Let Y be a random variable representing the edge length of a facet in the ridge network. If Y scales as \sqrt{X} , the consequent distribution of Y is a gamma distribution,

$$f_Y(y) = \frac{1}{\theta\Gamma(a)} \left(\frac{y}{\theta}\right)^{a-1} e^{-y/\theta}, \quad (9)$$

with θ the scale and a the shape parameter, alluded to in Section IV, and with mean edge length $a\theta$. The distributions of facet area and edge length provided by Eqs. (8) & (9) allow us to formulate an expression for the typical total crease length as a function of t , in tandem with the evolution of mean area $s(t)$. First, we briefly restate the key result of Ref. [16] to which we will compare our model. The total crease length ℓ was found to vary according to a logarithm of the number of crumpling and

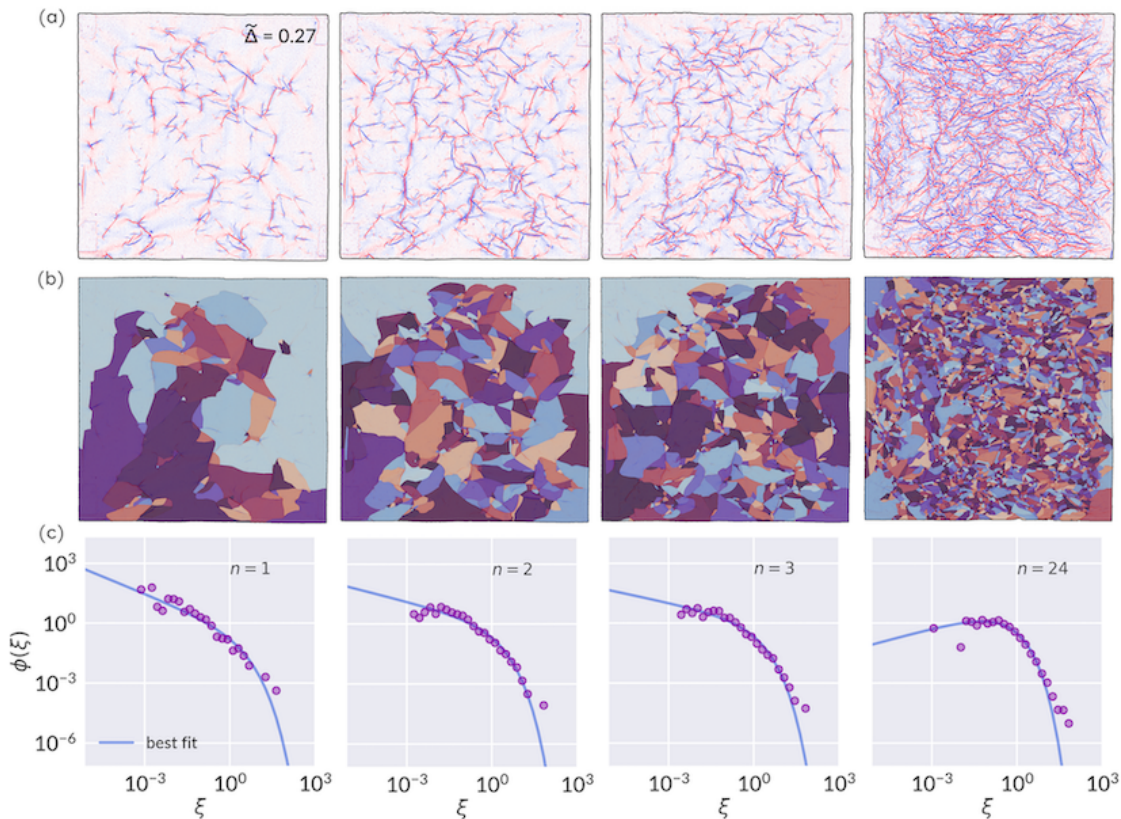


FIG. 3. (a) The map of mean curvature for iterations $n = 1, 2, 3$ and 24 of a sample sheet crumpled with compaction ratio $\tilde{\Delta} = 0.27$, and (b) the corresponding facet segmentation. (c) Experimental distributions of scaled facet area $\xi = x/s$ for each sample (scattered points) and best fit curve to Eq. (7a) (solid line), with fitting parameter a .

unfolding repetitions n :

$$\ell(n, \tilde{\Delta}) = c_1(1 - \tilde{\Delta}) \log \left(1 + \frac{c_2 n}{\tilde{\Delta}} \right), \quad (10)$$

with $\tilde{\Delta}$ the compaction ratio, and c_1 and c_2 fitting parameters. A striking property of this model is its implication that the rate at which new damage accumulates, as measured by added crease length per crumpling iteration $\delta\ell_{\tilde{\Delta}} \equiv \partial\ell/\partial n$, is uniquely determined by a sheet's instantaneous state $(n, \tilde{\Delta})$, and not by the prior history of its preparation. Moreover, the model is independent of the details of the crease network, such as the spatial homogeneity of damage across the sheet. The fitting parameters c_1 and c_2 are universal to all values of n and $\tilde{\Delta}$. Working with the moments of our derived facet area and edge length distributions, we can estimate the total length d of facet edges as the average length of an edge, $a\theta$, times the average number of edges. The latter may be expressed as the average number of facets, or the total sheet area divided by the typical facet area s , times the number of edges per facet n_e , halved to account for shared edges, which yields

$$d(t) = \frac{a\theta(t)}{s(t)} \times \frac{n_e}{2} = \frac{n_e t}{2(a+1)}. \quad (11)$$

A fit of Eq. (11) to the true sum of facet perimeters in the experimental samples reveals a value of $n_e \approx 4.6$, which suggests an average of 4–5 sides per facet. As shown in Fig. 4, d varies logarithmically with the number of crumpling repetitions n , in strong semblance to ℓ (Eq. (10)). We expect d and ℓ to be proportional, with differences arising due to incomplete scarring around facet perimeters as regions of the sheet restore elastically, particularly for mild compression. We find that $d(1 - \tilde{\Delta})$ accomplishes the desired proportionality and thereby completes our definition of ℓ as a function of t :

$$\ell(t, \tilde{\Delta}) = d(t)(1 - \tilde{\Delta}) = (1 - \tilde{\Delta}) \frac{n_e t}{2(a+1)}. \quad (12)$$

Importantly, the logarithmic scaling with discrete n is clearly reflected in d via the continuous variable t measuring the progression of fragmentation.

B. Numerical evidence for the insensitivity to initial preparation

Now that the connection between the statistical model of facet area and total crease length has been presented, we briefly note on the insight that may be gained by addi-

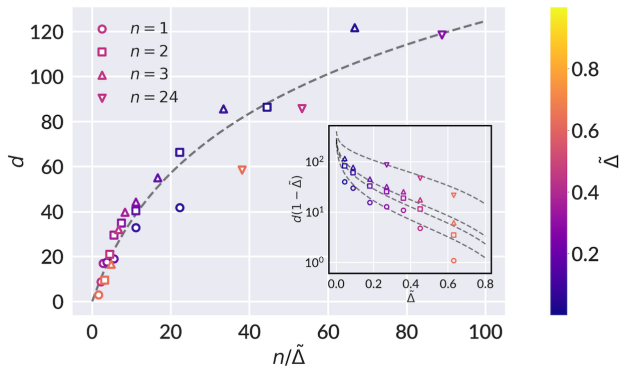


FIG. 4. Plot of d from Eq. (11) using the best fit shape parameter a for each experimental sample, against the corresponding ratio $n/\bar{\Delta}$ for the sample, which allows for a collapse of all points on the curve $y = c_1 \log(1 + c_2 x)$ shown by the dashed line. $c_1 = 52$ (normalized by 100 mm sheet size) and $c_2 = 0.1$, comparable to the best fit values in Ref. [16]: $c_1 = 5200$ mm, $c_2 = 0.063$. The inset shows an alternate validation of the relationship between Eqs. (10) and (11), plotting $d(1 - \bar{\Delta})$ as a function of $\bar{\Delta}$ with dashed lines corresponding to Eq. (10) for $n = 1$, $n = 2$, $n = 3$, and $n = 24$ in ascending order.

tionally solving Eq.(1) numerically. A numerical integration scheme is implemented using second-order composite trapezoid rule for discretization in x , and second-order implicit multi-step discretization in t . The sample numerical result in Fig. 5 reveals a rapid convergence to the steady state analytical solution given by Eqs. (7a) and (7b), and thereby relative insensitivity to the initial state. To demonstrate the significance of this behavior, we reiterate the observed history independence of total crease length. As discussed in Ref. [16], sheets with different loading histories—one hand-crumpled and another deliberately folded along straight lines—yet nearly equal total crease lengths exhibited the same subsequent accumulation of damage when subjected to the protocol of Fig. 1(a). Such sheets had clearly distinct initial facet area distributions: The facet areas of the deliberately folded sheet were sharply peaked near two different values, while those of the hand-crumpled sheet were broadly distributed. Thus, signatures of initial preparation appear to be quickly eclipsed by the strong attractor of the crumpled state, echoed in the rapid convergence to steady state seen numerically.

Thus far, we have established that an estimate of total crease length constructed from moments of the derived facet area and ridge length distributions shows consistency with the logarithmic scaling of Eq. (10). In the following section, we propose a simple mechanism for how the geometric incompatibility of a folded sheet and its confinement leads to further fragmentation, driving t forward. This argument establishes the evolution of t in accordance with n , and thus supplies the missing link to a physically-based model that corroborates experimental findings.

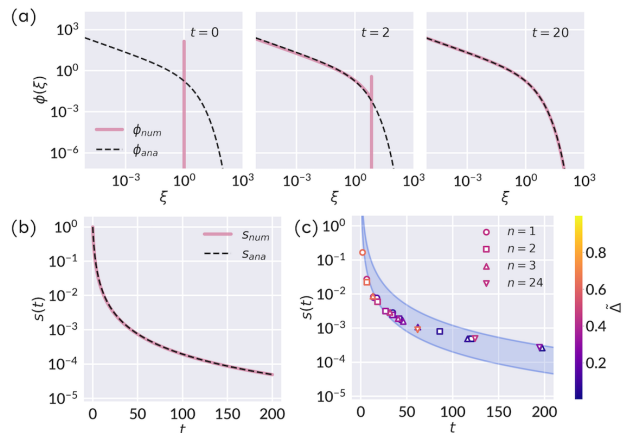


FIG. 5. Numerical validation of the analytical solution to Eq. (1). (a) Selected snapshots of the numerically calculated $\phi_{num}(\xi)$ with initial condition $c(x, 0) = \delta(x - 1)$ and with $a = 1$, revealing a rapid convergence to the steady state distribution. The dashed line corresponds to the analytical form of Eq. (7a) valid at large t . (b) The corresponding evolution of mean area $s(t)$, with the analytical solution given by Eq. (7b) shown by the dashed line. (c) The mean area of the experimental samples as a function of t computed from Eq. (7b) (scattered points). The best fit shape parameter a varies by sample; the shaded region is bounded by the curves of $s(t)$ corresponding to $a = 1$ and $a = 3$ for reference.

VI. ONE-DIMENSIONAL MODEL

To offer an explanation for the observed logarithmic scaling, we develop a simple one-dimensional model that proposes how additional fragments may form when a crumpled sheet is re-crumpled, relying on the statistical descriptions of facet area and segment length formulated in the previous sections. Our goal can be summarized by the following two questions: (1) Given its current state and prescribed confinement, with what probability does a sheet undergo further fragmentation? (2) How does this probability relate to the continuous variables in the fragmentation model of Eq. (1)? First, we appeal to the axial symmetry of our confinement to simplify our view of crumpling to a 1D strip of length L_0 , as shown in Fig. 6. The strip is characterized by a sequence of folds in alternating directions which divide the strip into random segments. The lengths r of the segments, which are equal to the cross-sections of the intercepted facets, are distributed according to the derived gamma distribution of Eq. (9), weighted by the horizontal facet width, which increases the likelihood of a facet's occurrence within a randomly selected vertical strip. For facets of approximately 1 : 1 aspect ratio, the distribution of segment length is thereby

$$f_R(r) = \frac{1}{\theta \Gamma(a+1)} \left(\frac{r}{\theta}\right)^a e^{-r/\theta}, \quad (13)$$

with the average segment length given by $(a+1)\theta$. A comparison of Eq. (13) with experimental data is provided

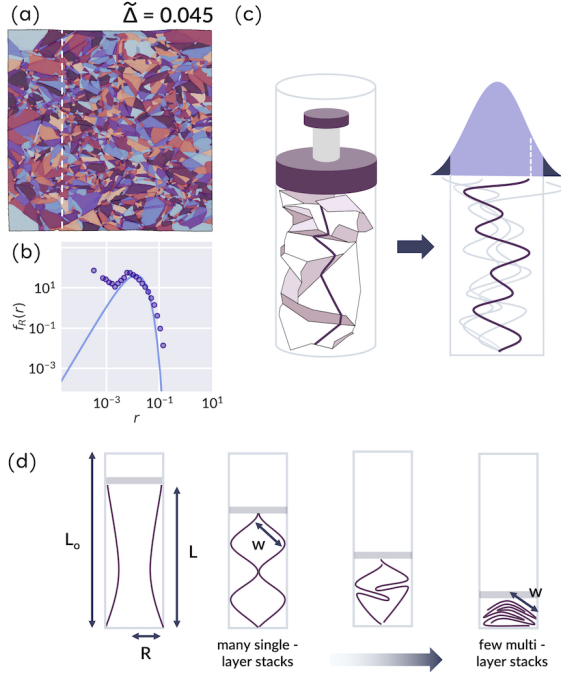


FIG. 6. (a) A sample segmented sheet with dashed line indicating a vertical cross section. (b) The distribution of segment lengths from all such cross-sections of the sheet in (a) (filled points), with Eq. (13) plotted as a solid curve. No additional fit is performed; the value of the shape parameter a which appears in Eq. (13) is taken from the best fit facet area distribution, Eq. (7a), for this sample. (c) A schematic of the analogue between the folding of a one-dimensional strip in an axially confined sheet and a one-dimensional random walk whose time axis is extended vertically for clarity. The filled curve represents the distribution of the walker's final displacement, with darker shaded regions denoting the fraction of walks which lie outside a given confinement. (d) Simplified illustration of one-dimensional folding which facilitates a geometric estimate of the critical confinement w presented in Eq. (S4) and further detailed in Section VI of the Supplemental Material [30].

for a strongly compacted sample in Fig. 6(a-b).

As a preliminary step, we derive the final displacement of the strip when folded at each break, in the absence of confinement. This problem can be mapped to the displacement of a walker performing a one-dimensional random walk with gamma-distributed steps. To enforce the concept of folding, the walker's steps occur in alternating directions. The distribution of position Z after $2k$ steps, derived in full in Section III of the Supplemental Material [30], is found to be

$$f_Z(z; a, \theta) = \frac{1}{\sqrt{\pi}\theta\Gamma(k(a+1))} \left(\frac{|z|}{2\theta}\right)^{-\nu} K_\nu\left(\frac{|z|}{\theta}\right), \quad (14)$$

where $\nu = \frac{1}{2} - k(a+1)$, $K_\nu(z)$ is the modified Bessel function of the second kind of order ν , and $\Gamma(k)$ is the gamma function. Note that $2k$ is related to the average segment length $(a+1)\theta$ as $2k = L_0/(a+1)\theta$ to preserve each walk's total length on average; this approximation improves with decreasing step size.

If a confinement is now introduced at the locations $|z| = w$, we next ask with what likelihood the walker steps beyond this confinement. One approach to approximate this probability is to integrate Eq. (14) for all $|z| > w$, producing a two-sided survival function of Eq. (14). Although this is not equivalent to our initial question, as intermediate steps may also have landed past $|z| > w$, it proves an acceptable estimate as the last step has the greatest variance. A more accurate calculation would be to evaluate the likelihood that a given walk escapes the confinement at *any* step; however, looking at the last step is useful for its simplicity in analytical form, and still captures the anticipated behavior. A comparison to the more accurate formulation is made numerically and provided in Section V of the Supplemental Material [30]. Integrating Eq. (14), we obtain a two-sided survival function $S_Z(w; a, \theta) = P(|Z| > w; w \geq 0)$ for a threshold confinement w which triggers fragmentation for all samples of $|z| > w$. The derivation of the exact form for $S_Z(w; a, \theta)$ is presented in Section III of the Supplemental Material [30], with the following result:

$$S_Z(w; a, \theta) = 1 + \frac{\sqrt{\pi}}{\Gamma(k(a+1))} \left(\frac{w}{\theta}\right) \csc(\pi\nu) \left[\frac{4^\nu}{(2\nu-1)\Gamma(1-\nu)} \left(\frac{w}{\theta}\right)^{-2\nu} {}_1F_2\left(\frac{1}{2} - \nu; 1 - \nu, \frac{3}{2} - \nu; \frac{1}{4}\left(\frac{w}{\theta}\right)^2\right) + \frac{1}{\Gamma(1+\nu)} {}_1F_2\left(\frac{1}{2}; \frac{3}{2}, 1 + \nu; \frac{1}{4}\left(\frac{w}{\theta}\right)^2\right) \right]. \quad (15)$$

In order for walkers at $|z| > w$ to be restored within the limits of confinement, one or more of their steps must fragment, thereby increasing the number of steps taken and decreasing the overall average, which drives the evolution of fragmentation. This articulates our key claim: Considering our original, cylindrically shaped sheets as

a statistical ensemble of one-dimensional random walks, we suggest that the progression of fragmentation measured by a change dt , over a single crumpling iteration dn , should be proportional to the fraction of walks in the ensemble which leave the confinement imposed at $|z| = w$: $dt/dn \sim S_Z(w; a, \theta)$. Equivalently, this is the

likelihood that a single random walk leaves the critical confinement. At present, Eq. (15) gives the likelihood that new creases will form; however, it does not yet describe how much new damage is created, for which two additional factors should be considered: (1) When the sheet is strongly confined in closely-packed layers, the layers tend to collectively fragment, as alluded to in Refs. [15] and [16], thus contributing a factor $p \sim 1/L$ such that halving the final height doubles the number of additional ridges. (2) In the opposite limit of low compaction, facets are not in close proximity and need not behave cooperatively; thus, new damage scales linearly with the amount of compression $L_0 - L$, as argued in Ref. [16]. With these additional considerations, we propose that the evolution of the fragmentation process with crumpling iteration behaves as

$$\delta t_{frag} \equiv \frac{\partial t}{\partial n} \sim \frac{1 - \tilde{\Delta}}{\tilde{\Delta}} S_Z(w; a, t). \quad (16)$$

We indicate the explicit dependence on t here, as t and θ are inversely related. The critical width w is determined by the geometry of the imposed confinement, as illustrated in Fig. 6(d); a complete derivation is provided in Section VI of the Supplemental Material [30]:

$$w(\tilde{\Delta}) \approx \frac{R}{\sqrt{1 - \tilde{\Delta}^2}}, \quad (17)$$

where R is the radius of the container. The change in total crease length with crumpling iteration given by the model of Ref. [16] and following from Eq. (10) is:

$$\delta \ell_{\tilde{\Delta}} \equiv \frac{\partial \ell}{\partial n} = \frac{c_1 c_2 (1 - \tilde{\Delta})}{\tilde{\Delta}} \exp \left\{ - \frac{\ell}{c_1 (1 - \tilde{\Delta})} \right\}. \quad (18)$$

By consequence of Eq. (12) we can obtain the corresponding rate of change of t as prescribed by Eq. (18):

$$\delta t_{log} = \frac{dt}{d\ell} \delta \ell_{\tilde{\Delta}} = \frac{2(a+1)}{n_e(1-\tilde{\Delta})} \delta \ell_{\tilde{\Delta}}. \quad (19)$$

Fig. 7 compares the agreement of Eq. (16) with the anticipated relation from Eq. (19). Parameters c_1 and c_2 are consistent with those presented in Fig. 4; the only fitting parameter introduced in the results of Fig. 7 is a constant of proportionality between Eqs. (16) & (19). Collectively, the results of Figs. 4 & 7 demonstrate clear consistency of the fragmentation model with the anticipated logarithmic growth.

VII. CONCLUSION

By pursuing a correspondence between the crumpling of a thin sheet and a general fragmentation process, we have derived a physically-based framework for the evolution of statistical properties of intricate crumpled patterns. Equipped with theoretical models in close agreement with

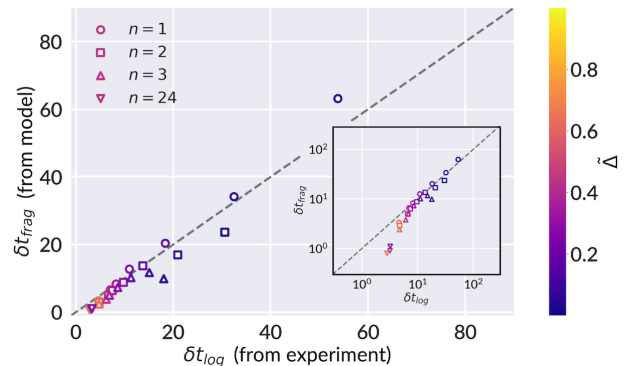


FIG. 7. Plot of the derived relation modeled by Eq. (16) against the anticipated experimental relation of Eq. (19) with fitted constant of proportionality. Each point is calculated using the best fit parameter a of the sample's facet area distribution. The dashed line corresponds to $y = x$ and is a guide to the eye. The points are shown on logarithmic axes in the inset for clarity at small values.

experimental data, we have proposed a simple model of one-dimensional folding in which further fragmentation ensues due to a geometric incompatibility between the sequence of folds and the imposed confinement, likened to a random walk exceeding a critical allowed displacement. The predicted accrual of damage, quantified by added crease length, shows strong consistency with the logarithmic model of Gottesman *et al.* [16], and thereby supplies a possible physical basis for the puzzling origin of logarithmic scaling in repeated crumpling experiments. Furthermore, our model explains the history independence of the logarithmic scaling, since the area distribution of the crumpled state is such a strong attractor in the fragmentation process.

The consistency of crumpling with fragmentation theory hints at the possibility of universal behavior uniting more diverse fragmenting systems. For example, the activation of defects in the fragmentation of ceramics can locally slow down subsequent fracture, and may bear semblance to the slowing of damage accumulation as a re-crumpled sheet exploits its existing folds [32]. Thus, studies of crumpled systems might offer a new lens through which to interpret other complex processes. An immediate extension of this work would be a validation of the results on sheets of varied thicknesses and material parameters, as well as those prepared according to different compaction protocols. Moreover, it may be of value to explore slight generalizations of proposed functional forms introduced in this study, such as the breakup rates; this could allow variations across other experimental results to be explained, such as those arising between low and high compaction regimes [12, 15], thereby providing a unifying framework for such observations.

Additionally, deeper understanding of crumpling dynamics can assist data-driven approaches to predicting damage network formation. Though machine learning

methods are capable of unveiling hidden structure in complex, disordered systems [33, 34], prior work has demonstrated the importance of preserving physical properties in making faithful predictions: for example, preserving vertex angle constraints in synthetic fold patterns to assist the task of ridge network reconstruction in crumpled sheets [35]. In addition to encoding physical rules implicitly through data, future machine learning approaches may explicitly enforce constraints such as facet area and crease length statistics in predicting ridge network evolution. Strategies which couple detailed spatial data with coarse-grained theoretical insight could thus enable more comprehensive predictions of crumpling dynamics in future studies.

ACKNOWLEDGMENTS

This work was supported by the National Science Foundation under Grant No. DMR-1420570. J.A. acknowledges support from the National Science Foundation under Grant No. DGE-1745303. C.H.R. was partially supported by the Applied Mathematics Program of the U.S. DOE Office of Science Advanced Scientific Computing Research under Contract No. DE-AC02-05CH11231.

Author contributions S.M.R and C.H.R conceived the study and supervised the project. L.M.L performed new experiments. J.A. performed the image segmentation. J.A. and C.H.R. carried out analytical derivations and numerical validation. J.A. and C.H.R. wrote the paper with input from all authors.

-
- [1] J. Zang, S. Ryu, N. Pugno, Q. Wang, Q. Tu, M. J. Buehler, and X. Zhao, Multifunctionality and control of the crumpling and unfolding of large-area graphene, *Nature Materials* **12**, 321 (2013).
- [2] V. Belousov, The origin of folding in the Earth's crust, *Journal of Geophysical Research* **66**, 2241 (1961).
- [3] J. Song, Z. Yu, M. L. Gordin, and D. Wang, Advanced sulfur cathode enabled by highly crumpled nitrogen-doped graphene sheets for high-energy-density lithium-sulfur batteries, *Nano letters* **16**, 864 (2016).
- [4] Z. Wen, X. Wang, S. Mao, Z. Bo, H. Kim, S. Cui, G. Lu, X. Feng, and J. Chen, Crumpled nitrogen-doped graphene nanosheets with ultrahigh pore volume for high-performance supercapacitor, *Advanced materials* **24**, 5610 (2012).
- [5] M. Kaltenbrunner, T. Sekitani, J. Reeder, T. Yokota, K. Kuribara, T. Tokuhara, M. Drack, R. Schwödianer, I. Graz, S. Bauer-Gogonea, *et al.*, An ultra-lightweight design for imperceptible plastic electronics, *Nature* **499**, 458 (2013).
- [6] M. S. White, M. Kaltenbrunner, E. D. Głowacki, K. Gutnichenko, G. Kettlgruber, I. Graz, S. Aazou, C. Ulbricht, D. A. Egbe, M. C. Miron, *et al.*, Ultrathin, highly flexible and stretchable plects, *Nature Photonics* **7**, 811 (2013).
- [7] S. Deboeuf, E. Katzav, A. Boudaoud, D. Bonn, and M. Adda-Bedia, Compaction of thin sheets: crumpling and folding, in *21st French Mechanics Congress, Bordeaux, FR* (2013).
- [8] S. Deboeuf, E. Katzav, A. Boudaoud, D. Bonn, and M. Adda-Bedia, Comparative study of crumpling and folding of thin sheets, *Physical Review Letters* **110**, 104301 (2013).
- [9] C. A. Andresen, A. Hansen, and J. Schmittbuhl, Ridge network in crumpled paper, *Physical Review E* **76**, 026108 (2007).
- [10] D. L. Blair and A. Kudrolli, Geometry of crumpled paper, *Physical Review Letters* **94**, 166107 (2005).
- [11] A. S. Balankin, O. S. Huerta, R. C. M. De Oca, D. S. Ochoa, J. M. Trinidad, and M. A. Mendoza, Intrinsically anomalous roughness of randomly crumpled thin sheets, *Physical Review E* **74**, 061602 (2006).
- [12] A. S. Balankin and O. S. Huerta, Entropic rigidity of a crumpling network in a randomly folded thin sheet, *Physical Review E* **77**, 051124 (2008).
- [13] A. S. Balankin, A. H. Rangel, G. G. Pérez, F. G. Martinez, H. S. Chavez, and C. L. Martinez-Gonzalez, Fractal features of a crumpling network in randomly folded thin matter and mechanics of sheet crushing, *Physical Review E* **87**, 052806 (2013).
- [14] G. Vliegenthart and G. Gompper, Forced crumpling of self-avoiding elastic sheets, *Nature Materials* **5**, 216 (2006).
- [15] E. Sultan and A. Boudaoud, Statistics of crumpled paper, *Physical Review Letters* **96**, 136103 (2006).
- [16] O. Gottesman, J. Andrejevic, C. H. Rycroft, and S. M. Rubinstein, A state variable for crumpled thin sheets, *Communications Physics* **1**, 70 (2018).
- [17] Y. Lahini, O. Gottesman, A. Amir, and S. M. Rubinstein, Nonmonotonic aging and memory retention in disordered mechanical systems, *Physical Review Letters* **118**, 085501 (2017).
- [18] A. S. Balankin, O. S. Huerta, F. H. Méndez, and J. P. Ortiz, Slow dynamics of stress and strain relaxation in randomly crumpled elasto-plastic sheets, *Physical Review E* **84**, 021118 (2011).
- [19] K. Matan, R. B. Williams, T. A. Witten, and S. R. Nagel, Crumpling a thin sheet, *Physical Review Letters* **88**, 076101 (2002).
- [20] A. Eisenbach, T. Havdala, J. Delahaye, T. Grenet, A. Amir, and A. Frydman, Glassy dynamics in disordered electronic systems reveal striking thermal memory effects, *Physical Review Letters* **117**, 116601 (2016).
- [21] A. Bérut, O. Pouliquen, and Y. Forterre, Creeping avalanches of brownian granular suspensions, *arXiv preprint arXiv:1710.09111* (2017).
- [22] P. Rosin, Laws governing the fineness of powdered coal, *Journal of Institute of Fuel* **7**, 29 (1933).
- [23] A. Kolmogoroff, Über das logarithmisch normale verteilungsgesetz der dimensionen der teilchen bei zerstückelung (translated as the logarithmically normal law of distribution of dimensions of particles when broken into small parts), in *CR (Doklady) Acad. Sci. URSS (NS)*, Vol. 31 (1941) pp. 99–101.
- [24] D. Grady, *Physics of Shock and Impact, Volume 1*, 2053-2563 (IOP Publishing, 2017).
- [25] W. K. Brown and K. H. Wohletz, Derivation of the Weibull distribution based on physical principles and

- its connection to the Rosin–Rammler and lognormal distributions, *Journal of Applied Physics* **78**, 2758 (1995).
- [26] W. K. Brown, A theory of sequential fragmentation and its astronomical applications, *Journal of Astrophysics and Astronomy* **10**, 89 (1989).
- [27] Z. Cheng and S. Redner, Kinetics of fragmentation, *Journal of Physics A: Mathematical and General* **23**, 1233 (1990).
- [28] M. Wang, J. Smith, and B. J. McCoy, Continuous kinetics for thermal degradation of polymer in solution, *AIChE Journal* **41**, 1521 (1995).
- [29] E. Kaminski and C. Jaupart, The size distribution of pyroclasts and the fragmentation sequence in explosive volcanic eruptions, *Journal of Geophysical Research: Solid Earth* **103**, 29759 (1998).
- [30] See supplemental material at [] for complete segmented data, comparison with automated segmentation, and detailed derivation of all analytical results presented in this work.
- [31] A. S. Balankin and L. Flores-Cano, Edwards’s statistical mechanics of crumpling networks in crushed self-avoiding sheets with finite bending rigidity, *Physical Review E* **91**, 032109 (2015).
- [32] S. Levy and J.-F. Molinari, Dynamic fragmentation of ceramics, signature of defects and scaling of fragment sizes, *Journal of the Mechanics and Physics of Solids* **58**, 12 (2010).
- [33] E. D. Cubuk, S. S. Schoenholz, J. M. Rieser, B. D. Malone, J. Rottler, D. J. Durian, E. Kaxiras, and A. J. Liu, Identifying structural flow defects in disordered solids using machine-learning methods, *Physical Review Letters* **114**, 108001 (2015).
- [34] J. Carrasquilla and R. G. Melko, Machine learning phases of matter, *Nature Physics* **13**, 431 (2017).
- [35] J. Hoffmann, Y. Bar-Sinai, L. M. Lee, J. Andrejevic, S. Mishra, S. M. Rubinstein, and C. H. Rycroft, Machine learning in a data-limited regime: Augmenting experiments with synthetic data uncovers order in crumpled sheets, *Science advances* **5**, eaau6792 (2019).
- [36] I. S. Gradshteyn, I. M. Ryzhik, and R. H. Romer, *Tables of integrals, series, and products* (1988).
- [37] Wolfram Research, Inc., *Mathematical Functions Site* (<http://functions.wolfram.com/03.04.21.0116.01>), Champaign, IL, 2019.
- [38] Wolfram Research, Inc., *Mathematical Functions Site* (<http://functions.wolfram.com/03.04.21.0011.01>), Champaign, IL, 2019.
- [39] NIST Digital Library of Mathematical Functions, Release 1.0.24 of 2019-09-15 (<http://dlmf.nist.gov/10.41.E4>), f. W. J. Olver, A. B. Olde Daalhuis, D. W. Lozier, B. I. Schneider, R. F. Boisvert, C. W. Clark, B. R. Miller, B. V. Saunders, H. S. Cohl, and M. A. McClain, eds.
- [40] Wolfram Research, Inc., *Mathematical Functions Site* (<http://functions.wolfram.com/06.05.06.0010.01>), Champaign, IL, 2019.

Supplemental material for ‘A model for the fragmentation kinetics of crumpled thin sheets’

Jovana Andrejevic,¹ Lisa M. Lee,¹ Shmuel M. Rubinstein,¹ and Chris H. Rycroft^{1,2}

¹*John A. Paulson School of Engineering and Applied Sciences,
Harvard University, Cambridge, MA 02138, USA*

²*Computational Research Division, Lawrence Berkeley Laboratory, Berkeley, CA 94720, USA*

I. SCALING SOLUTION TO THE FRAGMENTATION RATE EQUATION

Facet fragmentation is modeled following the theory of fragmentation kinetics outlined in Ref. [27]. Here we reproduce the derivation of a scaling solution shared among setups with similar families of breakup rates, as well as carry out the analytical steps unique to our specific choice of these rates. The linear integro-differential equation describing the evolution of concentration of facet areas x , $c(x, t)$, is given by:

$$\frac{\partial c(x, t)}{\partial t} = \underbrace{-r(x)c(x, t)}_{\text{depletion of facets of area } x} + \int_x^\infty \underbrace{c(y, t)r(y)f(x|y)dy}_{\text{gain in facets of area } x}, \quad (\text{S1})$$

where

t	measure of progression of fragmentation
$r(x)$	overall rate at which a facet of area x breaks
$f(x y)$	conditional probability that x is produced from the breakup of y , $y \geq x$
$c(x, t)$	concentration of facets of area x

with the scaling ansatz

$$c(x, t) = \frac{1}{s^2} \phi\left(\frac{x}{s}\right),$$

which restricts all time dependence to a parameter $s = s(t)$ that represents the typical (mean) area, and $\phi(\xi)$ is a scaling function. The scaling function satisfies

$$\int_0^\infty \phi(\xi) d\xi = 1$$

$$\int_0^\infty \xi \phi(\xi) d\xi = 1$$

such that

$$\int_0^\infty c(x, t) dx = \frac{1}{s(t)} \quad (\text{average number of facets})$$

$$\int_0^\infty xc(x, t) dx = 1 \quad (\text{total area}),$$

which ensures conservation of area. A common choice of $r(x)$ and $f(x|y)$ which prove analytically tractable are members of homogeneous kernels:

$$r(x) = x^\lambda,$$

$$f(x|y) = \frac{1}{y} b\left(\frac{x}{y}\right).$$

With this formulation, larger facets are more likely to split due to the higher rate given by $r(x)$ assuming $\lambda > 0$. Moreover, the conditional probability must satisfy area conservation,

$$\int_0^y xf(x|y) dx = y.$$

Plugging the scaling ansatz and general homogeneous kernels into the rate equation, and defining $\xi = x/s, \eta = y/s$ yields

$$\begin{aligned} \frac{\partial \left(\frac{1}{s^2} \phi(\xi) \right)}{\partial t} &= -x^\lambda \frac{1}{s^2} \phi(\xi) + \int_x^\infty \frac{1}{s^2} \phi(\eta) y^\lambda \frac{1}{y} b\left(\frac{\xi}{\eta}\right) dy, \\ -\frac{2}{s^3} \dot{s} \phi(\xi) + \frac{1}{s^2} \phi'(\xi) \left(-\frac{x}{s^2} \right) \dot{s} &= -s^{\lambda-2} \xi^\lambda \phi(\xi) + \int_\xi^\infty s^{\lambda-2} \phi(\eta) \eta^{\lambda-1} b\left(\frac{\xi}{\eta}\right) d\eta, \\ -\dot{s} s^{-(\lambda+1)} \left(2\phi(\xi) + \xi \phi'(\xi) \right) &= -\xi^\lambda \phi(\xi) + \int_\xi^\infty \phi(\eta) \eta^{\lambda-1} b\left(\frac{\xi}{\eta}\right) d\eta, \end{aligned}$$

where $\dot{s} \equiv ds/dt$. By separating the dependence on x and t we must have that

$$-\dot{s} s^{-(\lambda+1)} = \frac{-\xi^\lambda \phi(\xi) + \int_\xi^\infty \phi(\eta) \eta^{\lambda-1} b\left(\frac{\xi}{\eta}\right) d\eta}{2\phi(\xi) + \xi \phi'(\xi)} = \omega = \text{constant}$$

and thus have two equations

$$\dot{s} s^{-(\lambda+1)} = -\omega, \tag{S2a}$$

$$\omega \left(2\phi(\xi) + \xi \phi'(\xi) \right) = -\xi^\lambda \phi(\xi) + \int_\xi^\infty \phi(\eta) \eta^{\lambda-1} b\left(\frac{\xi}{\eta}\right) d\eta \tag{S2b}$$

Insight from individual facet fragmentation reveals a suitable form for the conditional breakup rate:

$$b\left(\frac{x}{y}\right) = \left(\frac{\beta+2}{\beta+1}\right) \rho\left(\frac{x}{y}\right),$$

where

$$\begin{aligned} \rho\left(\frac{x}{y}\right) &= (\beta+1) \left(\frac{x}{y}\right)^\beta, \\ \beta &= \frac{a}{2} - 1, \end{aligned}$$

and $\rho(x/y)$ is the probability density function of facet areas x normalized by their parent facet's area y from the previous crumpling iteration. In other words, $\rho(x/y)d(x/y)$ is the probability that a facet breaks to produce a fragment that is x/y of its initial area. This formulation introduces the assumption that fragmentation is a scale invariant process.

Next we demonstrate the agreement of our scaling function with the rate equation. We have that

$$\begin{aligned} \phi(\xi) &= \frac{\lambda}{\Gamma\left(\frac{a}{2\lambda}\right)} G(a, \lambda) (G(a, \lambda) \xi)^{\frac{a}{2}-1} e^{-(G(a, \lambda) \xi)^\lambda}, \\ \phi'(\xi) &= \frac{\lambda}{\Gamma\left(\frac{a}{2\lambda}\right)} G^2(a, \lambda) \left[\left(\frac{a}{2} - 1\right) (G(a, \lambda) \xi)^{\frac{a}{2}-2} - \lambda (G(a, \lambda) \xi)^{\frac{a}{2}+\lambda-2} \right] e^{-(G(a, \lambda) \xi)^\lambda} \\ &= \left[\left(\frac{a}{2} - 1\right) - \lambda (G(a, \lambda) \xi)^\lambda \right] \frac{\phi(\xi)}{\xi} \end{aligned}$$

for $G(a, \lambda) = \Gamma\left(\frac{a+2}{2\lambda}\right)/\Gamma\left(\frac{a}{2\lambda}\right)$. Substituting in $b(x/y)$, we have that

$$\begin{aligned} \int_\xi^\infty \phi(\eta) \eta^{\lambda-1} b\left(\frac{\xi}{\eta}\right) d\eta &= \frac{\lambda}{\Gamma\left(\frac{a}{2\lambda}\right)} G(a, \lambda) \left(\frac{a}{2} + 1\right) (G(a, \lambda) \xi)^{\frac{a}{2}-1} \int_\xi^\infty \eta^{\lambda-1} e^{-(G(a, \lambda) \eta)^\lambda} d\eta \\ &= \frac{1}{\Gamma\left(\frac{a}{2\lambda}\right)} \left(G(a, \lambda)\right)^{1-\lambda} \left(\frac{a}{2} + 1\right) (G(a, \lambda) \xi)^{\frac{a}{2}-1} e^{-(G(a, \lambda) \xi)^\lambda} \\ &= \frac{1}{\lambda} \left(G(a, \lambda)\right)^{-\lambda} \left(\frac{a}{2} + 1\right) \phi(\xi) \end{aligned}$$

Eq. (S2b) may be solved to obtain

$$\begin{aligned} \omega \left(2\phi(\xi) + \left[\left(\frac{a}{2} - 1 \right) - \lambda(G(a, \lambda)\xi)^\lambda \right] \phi(\xi) \right) &= -\xi^\lambda \phi(\xi) + \frac{1}{\lambda} \left(G(a, \lambda) \right)^{-\lambda} \left(\frac{a}{2} + 1 \right) \phi(\xi), \\ \omega \left(\frac{a}{2} + 1 - \lambda(G(a, \lambda)\xi)^\lambda \right) \phi(\xi) &= \frac{1}{\lambda} \left(G(a, \lambda) \right)^{-\lambda} \left(\frac{a}{2} + 1 - \lambda(G(a, \lambda)\xi)^\lambda \right) \phi(\xi) \end{aligned}$$

which is solved for all ξ when

$$\omega = \frac{1}{\lambda} \left(G(a, \lambda) \right)^{-\lambda}.$$

Moving to Eq. (S2a), we therefore have that

$$\begin{aligned} \dot{s} s^{-(\lambda+1)} &= -\frac{1}{\lambda} \left(G(a, \lambda) \right)^{-\lambda}, \\ \int_{s_0}^s s'^{-(\lambda+1)} ds' &= -\int_0^t \frac{1}{\lambda} \left(G(a, \lambda) \right)^{-\lambda} dt', \\ -\frac{1}{\lambda} \left(s^{-\lambda} - s_0^{-\lambda} \right) &= -\frac{1}{\lambda} \left(G(a, \lambda) \right)^{-\lambda} t, \\ s &= \left(\left(G(a, \lambda) \right)^{-\lambda} t + s_0^{-\lambda} \right)^{-1/\lambda} \end{aligned}$$

noting that $\lambda > 0$ in the case considered. The initial condition $s_0 = 1$ may be substituted for a fragmentation process originating from a single facet. However, in the limit of large t , the dependence of the typical area becomes insensitive to the initial condition, and our result may be simplified to $s(t) = \left(G(a, \lambda) \right) / t^\lambda$.

For the special case of $\lambda = 1/2$ considered in the main results of this work,

$$G \left(a, \lambda = \frac{1}{2} \right) = a(a+1), \tag{S3a}$$

$$\phi(\xi) = \frac{a(a+1)}{2\Gamma(a)} (a(a+1)\xi)^{\frac{a}{2}-1} e^{-\sqrt{a(a+1)}\xi}, \tag{S3b}$$

$$s(t) = \frac{a(a+1)}{t^2}. \tag{S3c}$$

II. COMPLETE DATA

A. Manual segmentation

As noted in the main text, final segmentation of all collected crease networks was performed by hand. These segmentations and the distributions of scaled facet areas are provided in Figs. S1 & S2, respectively.

B. Watershed segmentation

Prior to manual segmentation, an automated method using the watershed algorithm was initially tested. However, several concerns prompted a more careful labeling by hand. Firstly, the separation of creases from background was performed using a custom technique referred to as the Radon transform method, detailed in the Supplementary Discussion of Ref. [16]. This technique combines global and local thresholding to accommodate variations in the intensity (curvature) of creases; nevertheless, softening of old creases near strongly imprinted ones weakens their detection. The watershed algorithm proved sensitive to creases which scar the sheet but do not form closed contours, particularly true at low confinement (high $\tilde{\Delta}$). Thus, the algorithm over-partitions the crease network in these cases. Mitigating the effect of smaller, isolated creases and vertices by stricter thresholding also compromises the detection of

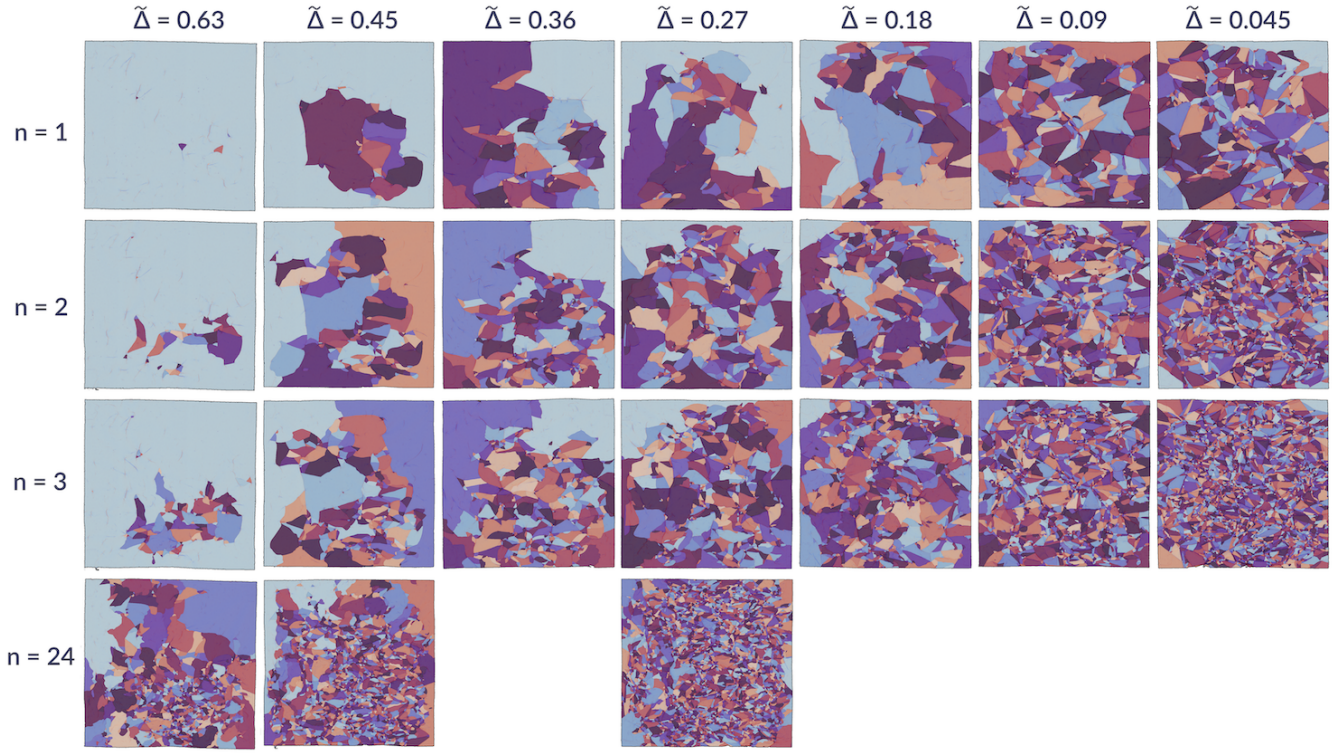


FIG. S1. Scans of crumpled sheets manually segmented into individual facets delineated by creases. Each column features a single sheet crumpled repeatedly n times to a specified compaction ratio $\tilde{\Delta} = L/L_0$.

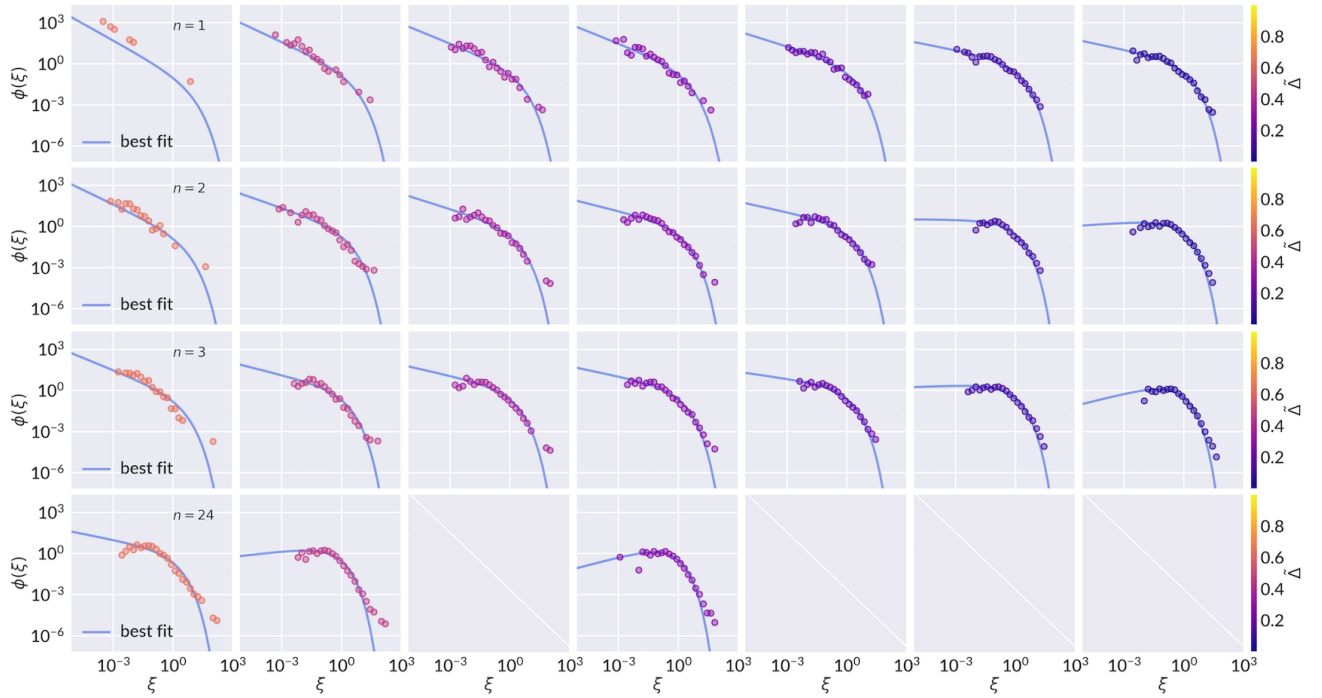


FIG. S2. Distributions of facet areas x normalized by the mean area s respectively for each sample. The solid line shows the best fit to Eq. (S3b) with single fitting parameter a for $\xi = x/s$.

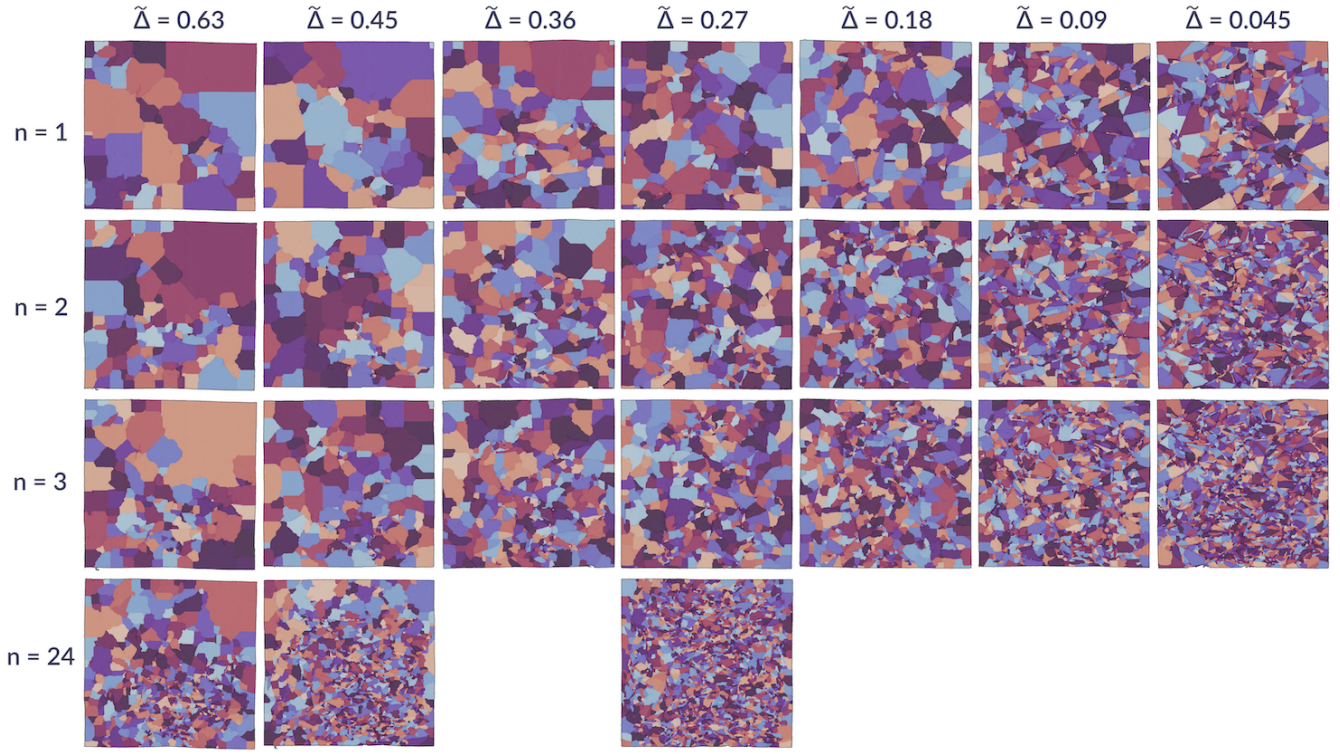


FIG. S3. Alternate segmentation to that presented in Fig. S1, performed in an automated manner using the watershed algorithm.

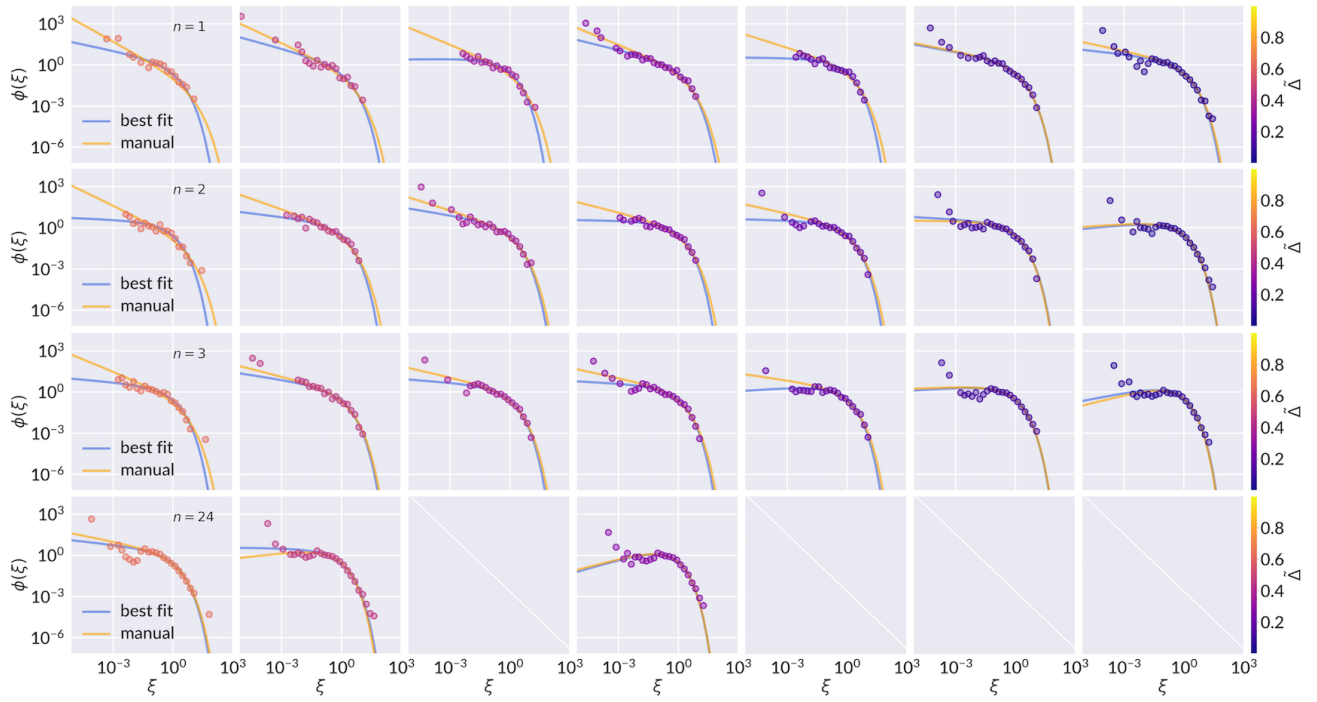


FIG. S4. Corresponding distributions of normalized facet areas ξ for the data in Fig. S3, with best fit to Eq. (S3b). The corresponding best fit from manual segmentation is also overlaid for reference.

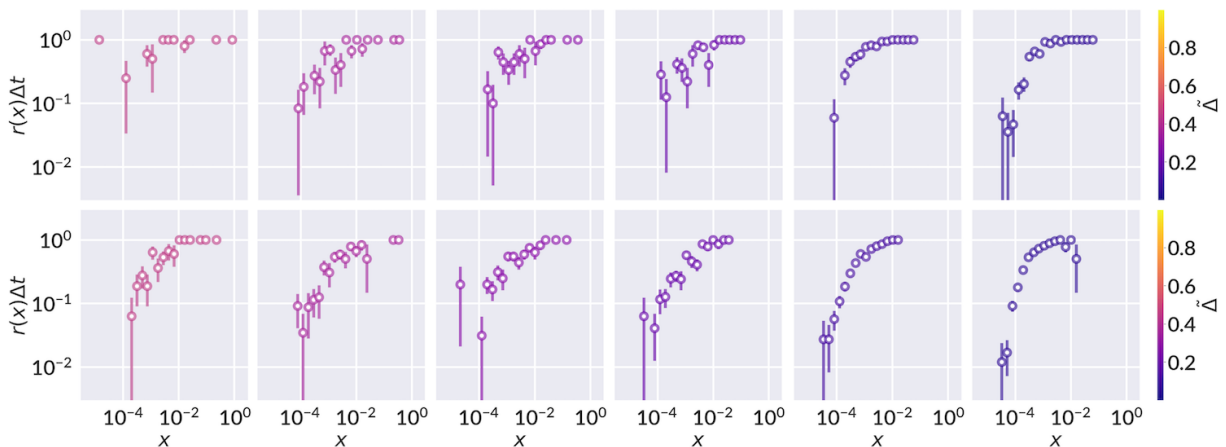


FIG. S5. The fraction of facets present after crumpling iteration $n = 1$ which fragment after $n = 2$ (top row) and the fraction of all facets at $n = 2$ which fragment after $n = 3$ (bottom row), for samples with $\tilde{\Delta} = 0.45, 0.36, 0.27, 0.18, 0.09$, and 0.045 (across). The sample with $\tilde{\Delta} = 0.63$ had too few facets to form a sufficient representative sample.

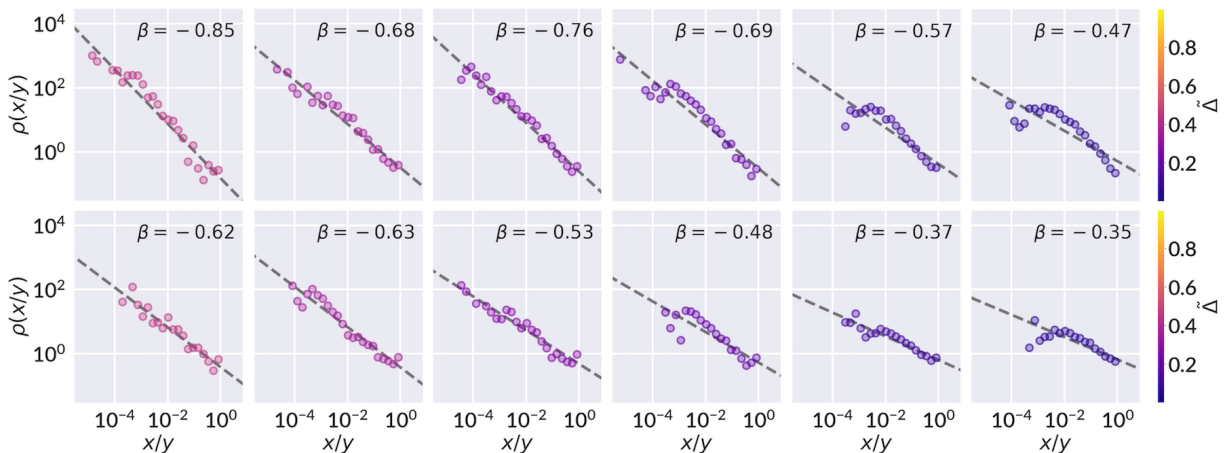


FIG. S6. The probability density function $\rho(x/y)$ of facet areas x present in crumpling iteration $n = 2$ normalized by their parent facet's area y from $n = 1$ (top row), and $\rho(x/y)$ of facet areas in $n = 3$ normalized by their parent facet's area from $n = 2$ (bottom row), for samples with $\tilde{\Delta} = 0.45, 0.36, 0.27, 0.18, 0.09$, and 0.045 (across). The sample with $\tilde{\Delta} = 0.63$ had too few facets to form a sufficient representative sample and is likewise excluded here.

smaller facets, impacting densely scarred samples at low $\tilde{\Delta}$. The results of watershed segmentation and corresponding scaled facet area distributions are presented in Figs. S3 and S4; while there is consistency with the manually segmented data, lower resolution and weaker performance for small features impacts the range over which consistent scaling is observed.

C. Breakup rates

Figure 2 in Section IV of the main text presents sample experimental evidence for the chosen forms of breakup rates $r(x)$ and $f(x|y)$. Figs. S5 and S6 present complete results for each value of $\tilde{\Delta}$ considered except $\tilde{\Delta} = 0.63$, for which there were too few facets per sheet to form a sufficient representative sample. While strongly compacted sheets provide a large supply of facets from which to build each distribution, they also undergo a succession of multiple fragmentation events in a single crumpling iteration, which obscures the behavior of individual facets. This impacts the observed trend in $\rho(x/y)$, for example, which departs from a power law relationship and begins to reflect the more mature facet area distribution of repeatedly crumpled sheets.

III. DISPLACEMENT OF A 1-D RANDOM WALK

For a random walk in one dimension comprised of random displacements R_i , the displacement from the origin after $2k$ steps is

$$D_{2k} = \sum_{i=1}^{2k} R_i$$

If consecutive steps occur in opposite directions, representing a fold, then individual steps can be grouped into k right (positive) and k left (negative) steps:

$$D_{2k} = R_k^+ - R_k^- \quad \text{where} \quad R_k^+ = \sum_{i=1,3,5\dots}^{2k} R_i, \quad R_k^- = \sum_{i=2,4,6\dots}^{2k} |R_i|$$

for each r_i drawn from the same distribution. If segment lengths $|R_i|$ are drawn from a gamma distribution with shape parameter $a + 1$ and scale parameter θ , consistent with the distribution of facet lengths traversed by a one-dimensional vertical cross-section, then R_k^+ and R_k^- are each distributed according to a gamma distribution with shape parameter $k(a + 1)$ and scale parameter θ :

$$|R_i| \sim \Gamma(a + 1, \theta), \quad R_k^+ \sim \Gamma(k(a + 1), \theta), \quad R_k^- \sim \Gamma(k(a + 1), \theta)$$

Thus D_{2k} is the difference of two identically distributed gamma variates. We can obtain the probability density function for D_{2k} through a convolution of the probability density functions of R_k^+ and $-R_k^-$. Let $X = R_k^+$, $Y = R_k^-$, and $Z = D_{2k}$; then

$$\begin{aligned} f_Z(z) &= f_{X-Y}(z) = \int_{-\infty}^{\infty} f_X(x) f_{(-Y)}(z - x) dx \\ &= \int_{-\infty}^{\infty} f_X(x) f_Y(x - z) dx. \end{aligned}$$

As $f_X(x)$ and $f_Y(y)$ both have non-negative support,

$$f_Z(z) = \begin{cases} \int_0^{\infty} f_X(x) f_Y(x - z) dx & \text{for } z \leq 0, \\ \int_0^{\infty} f_X(y + z) f_Y(y) dy & \text{for } z > 0, \end{cases}$$

where we have chosen the integration variable in the convolution to ensure the arguments of the probability density functions remain positive. With identical gamma distributions

$$\begin{aligned} f_X(x) &= \frac{1}{\theta \Gamma(k(a + 1))} \left(\frac{x}{\theta}\right)^{k(a+1)-1} e^{-x/\theta}, \\ f_Y(y) &= \frac{1}{\theta \Gamma(k(a + 1))} \left(\frac{y}{\theta}\right)^{k(a+1)-1} e^{-y/\theta}, \end{aligned}$$

where $\Gamma(k)$ is the gamma function,

$$f_Z(z) = \begin{cases} \frac{e^{z/\theta}}{\theta^2 \Gamma(k(a + 1))^2} \int_0^{\infty} \left(\frac{x}{\theta}\right)^{k(a+1)-1} \left(\frac{x - z}{\theta}\right)^{k(a+1)-1} e^{-2x/\theta} dx & \text{for } z \leq 0, \\ \frac{e^{-z/\theta}}{\theta^2 \Gamma(k(a + 1))^2} \int_0^{\infty} \left(\frac{y}{\theta}\right)^{k(a+1)-1} \left(\frac{y + z}{\theta}\right)^{k(a+1)-1} e^{-2y/\theta} dy & \text{for } z > 0. \end{cases}$$

The integral above may be solved using the following identity [36]:

$$\int_0^{\infty} x^{\nu-1} (x + \beta)^{\nu-1} e^{-\mu x} dx = \frac{1}{\sqrt{\pi}} \left(\frac{\beta}{\mu}\right)^{\nu-\frac{1}{2}} e^{\beta\mu/2} \Gamma(\nu) K_{\frac{1}{2}-\nu} \left(\frac{\beta\mu}{2}\right),$$

where $K_\nu(z)$ is the modified Bessel function of the second kind of order ν . This gives

$$f_Z(z) = \frac{1}{\sqrt{\pi}\theta\Gamma(k(a+1))} \left(\frac{|z|}{2\theta}\right)^{k(a+1)-\frac{1}{2}} K_{\frac{1}{2}-k(a+1)}\left(\frac{|z|}{\theta}\right).$$

$f_Z(z)$ should be a valid probability density function, and we can verify it indeed integrates to 1 over its support $z \in [0, \infty)$ using the following identity [37]:

$$\int_0^\infty t^{\alpha-1} K_\nu(t) dt = 2^{\alpha-2} \Gamma\left(\frac{\alpha-\nu}{2}\right) \Gamma\left(\frac{\alpha+\nu}{2}\right).$$

By symmetry about $z = 0$ we can integrate the following:

$$\begin{aligned} & \frac{2}{\sqrt{\pi}\Gamma(k(a+1))} \left(\frac{1}{2}\right)^{k(a+1)-\frac{1}{2}} \int_0^\infty \left(\frac{z}{\theta}\right)^{k(a+1)-\frac{1}{2}} K_{\frac{1}{2}-k(a+1)}\left(\frac{z}{\theta}\right) d\left(\frac{z}{\theta}\right) \\ &= \frac{2}{\sqrt{\pi}\Gamma(k(a+1))} \left(\frac{1}{2}\right)^{k(a+1)-\frac{1}{2}} 2^{k(a+1)-\frac{3}{2}} \Gamma\left(\frac{2k(a+1)}{2}\right) \Gamma\left(\frac{1}{2}\right) \\ &= \frac{\Gamma(k(a+1))\Gamma(1/2)}{\sqrt{\pi}\Gamma(k(a+1))} = 1 \end{aligned}$$

as $\Gamma(1/2) = \sqrt{\pi}$. Furthermore, for gamma-distributed steps, the average segment length is given by $(a+1)\theta$. Thus, in our system of a one-dimensional folded strip of total length L_0 , k and θ are related as

$$k = \frac{L_0}{2(a+1)\theta}$$

for a strip folded into $2k$ segments. Note that the total length of the walk is distributed as

$$\sum_{i=1}^{2k} |R_i| \sim \Gamma(2k(a+1), \theta)$$

and thus has mean $2k(a+1)\theta = L_0$ and variance $2k(a+1)\theta^2 = L_0\theta$ which tends to zero for small step sizes, improving the approximation of total length. By using the following identity [38],

$$\begin{aligned} \int z^{-\nu} K_\nu(z) dz &= -2^{-\nu-1} \pi z \csc(\pi\nu) \left[\frac{4^\nu z^{-2\nu}}{(2\nu-1)\Gamma(1-\nu)} {}_1F_2\left(\frac{1}{2}-\nu; 1-\nu; \frac{3}{2}-\nu; \frac{z^2}{4}\right) \right. \\ &\quad \left. + \frac{1}{\Gamma(\nu+1)} {}_1F_2\left(\frac{1}{2}; \frac{3}{2}; \nu+1; \frac{z^2}{4}\right) \right] + \text{constant}, \end{aligned}$$

$f_Z(z)$ may be integrated analytically to obtain an expression for a two-sided survival function as

$$\begin{aligned} S_Z(w; a, \theta) &= P(|Z| > w; w \geq 0) \\ &= 1 - 2 \int_0^w f_Z(z) dz \\ &= 1 + \frac{\sqrt{\pi}}{\Gamma(k(a+1))} \left(\frac{w}{\theta}\right) \csc(\pi\nu) \left[\frac{4^\nu}{(2\nu-1)\Gamma(1-\nu)} \left(\frac{w}{\theta}\right)^{-2\nu} {}_1F_2\left(\frac{1}{2}-\nu; 1-\nu; \frac{3}{2}-\nu; \frac{1}{4}\left(\frac{w}{\theta}\right)^2\right) \right. \\ &\quad \left. + \frac{1}{\Gamma(1+\nu)} {}_1F_2\left(\frac{1}{2}; \frac{3}{2}; 1+\nu; \frac{1}{4}\left(\frac{w}{\theta}\right)^2\right) \right], \end{aligned}$$

where $\nu = \frac{1}{2} - k(a+1)$.

IV. ASYMPTOTIC APPROXIMATION

To facilitate interpreting $f_Z(z)$ in a simpler mathematical form, we perform an asymptotic approximation in the limit of small θ , or large t . First, we recall that $k(a+1) = L_0/2\theta = L_0 t/2$. Using the parity of the modified Bessel

function of the second kind in its order parameter, $K_\nu(z) = K_{-\nu}(z)$, and substituting for $k(a+1)$, we have that

$$f_Z(z) = \frac{t}{\sqrt{\pi}\Gamma(L_0 t/2)} \left(\frac{|z|t}{2}\right)^{(L_0 t-1)/2} K_{(L_0 t-1)/2}(|z|t)$$

As both the order parameter and argument of the Bessel function grow in the limit of large t , we use the uniform asymptotic expansion, to leading order [39, Eq. 10.41.4]:

$$K_\nu(\nu z) \sim \left(\frac{\pi}{2\nu}\right)^{\frac{1}{2}} \frac{e^{-\nu\eta}}{(1+z^2)^{\frac{1}{4}}}$$

where

$$\eta = (1+z^2)^{\frac{1}{2}} + \log\left(\frac{z}{1+(1+z^2)^{\frac{1}{2}}}\right)$$

we let $\nu = (L_0 t - 1)/2$ and approximate

$$\begin{aligned} K_{(L_0 t-1)/2}(|z|t) &= K_\nu\left(\frac{|z|}{L_0}(2\nu+1)\right) \\ &\approx K_\nu\left(\frac{2\nu|z|}{L_0}\right) \text{ as } \nu \rightarrow \infty \\ &\sim \left(\frac{\pi}{2\nu\alpha}\right)^{\frac{1}{2}} e^{-\nu\eta}, \end{aligned}$$

where

$$\eta = \alpha + \log\left(\frac{2|z|/L_0}{1+\alpha}\right), \quad \alpha = (1+(2|z|/L_0)^2)^{\frac{1}{2}}.$$

We also use the asymptotic approximation of the gamma function [40],

$$\Gamma(z) \propto \sqrt{2\pi} z^{z-\frac{1}{2}} e^{-z} \text{ as } z \rightarrow \infty,$$

and thus

$$\Gamma\left(\frac{L_0 t}{2}\right) \propto \sqrt{2\pi} \left(\frac{L_0 t}{2}\right)^{(L_0 t-1)/2} e^{-L_0 t/2}.$$

Substituting in the two expansions, we have that

$$\begin{aligned} f_Z(z) &\sim \frac{t}{\pi\sqrt{2}} \left(\frac{L_0 t}{2}\right)^{-\nu} \left(\frac{|z|t}{2}\right)^\nu \left(\frac{\pi}{2\nu\alpha}\right)^{\frac{1}{2}} \left(\frac{2|z|/L_0}{1+\alpha}\right)^{-\nu} e^{L_0 t/2} e^{-\nu\alpha} \\ &= \frac{t}{\pi\sqrt{2}} \left(\frac{\pi}{2\nu\alpha}\right)^{\frac{1}{2}} \left(\frac{1+\alpha}{2}\right)^\nu e^{L_0 t/2 - \nu\alpha} \end{aligned}$$

and again approximating $2\nu+1 \approx 2\nu$ for large ν , we obtain

$$f_Z(z) \approx \sqrt{\frac{t}{2L_0\pi\alpha}} \left(\frac{1+\alpha}{2}\right)^{L_0 t/2} e^{-L_0 t(\alpha-1)/2}$$

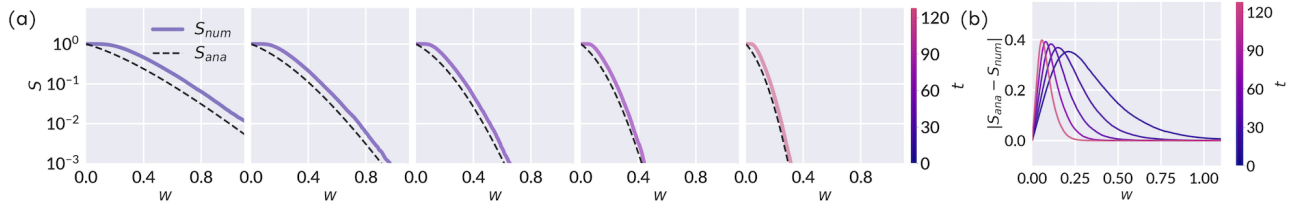


FIG. S7. (a) Plot of Eq. (15) which presents an analytical estimate of the fraction of escaped walk looking only at final displacements (dashed line), compared against the more accurate result obtained by assessing all intermediate displacements through numerical simulation (solid line). Simulations of 50,000 random walks, with gamma-distributed steps sampled according to Eq. (13) with shape parameter $a = 1$, are performed with $2k = 4, 8, 16, 32$, and 64 steps, and θ appropriately determined from the relation $\theta = L_0/2k(a + 1)$. The analytical approximation systematically underestimates the number of escaped walks by approximately a constant factor; thus, $S_Z(w; a, \theta)$ remains proportional to the change in t over a crumpling iteration in both the analytically approximate and numerically calculated forms, allowing variation in the constant of proportionality.

V. COMPARISON TO CONFINEMENT AT EACH STEP

As noted in Section VI of the main text, the survival function $S_Z(w; a, \theta)$ which gives the likelihood of a random walk as detailed in Section III of the Supplemental terminating past a critical confinement w , uses the final displacement of the walker, instead of all intermediate steps, to allow for analytical derivation. Fig. S7 compares the analytically derived approximation $S_Z(w; a, \theta)$ to the more accurate measure of the fraction of escaped walks determined by numerical simulation.

VI. CRITICAL CONFINEMENT

Our model of a folded one-dimensional strip as a random walk relates geometric incompatibility to the random walk stepping outside a confinement distance w . This critical distance w is dictated by the geometry of the imposed confinement, and the way in which the one-dimensional strip folds into *stacks* of one or more folded *layers* to accommodate its full length within the allowed space. Let m represent the number of spaced stacks, and p the average number of layers per stack, in our strip of length L_0 , confined to a rectangular container of width R and height L , $L \leq L_0$. To satisfy the constraint of total length L_0 at any compaction $\tilde{\Delta} = L/L_0$, we must have $mp\sqrt{(L/m)^2 + R^2} = L_0$. The critical width w of facets which would fragment under further confinement is given by $w = L_0/mp = \sqrt{(L/m)^2 + R^2}$. At low confinement, $p \approx 1$, and thus our constraint gives $m = (L_0/R)\sqrt{1 - \tilde{\Delta}^2}$, resulting in

$$w(\tilde{\Delta}) = \frac{R}{\sqrt{1 - \tilde{\Delta}^2}}. \quad (\text{S4})$$

At high confinement, the collapse of stacks leads to a decrease in m that scales in proportion to L , in turn scaling the number of layers $p \sim 1/L$. Specifically, we can define

$$\begin{aligned} m(\tilde{\Delta} \rightarrow 0) &\sim \frac{L}{R}, \\ p(\tilde{\Delta} \rightarrow 0) &\sim \frac{L_0}{L} \end{aligned}$$

and obtain

$$w(\tilde{\Delta} \rightarrow 0) = \frac{L_0}{mp} \sim R$$

which is consistent with our result at low confinement taken to the limit of small L . Thus we use Eq. (S4) throughout.